

ARTICLE OPEN

Mapping the elastic properties of two-dimensional MoS₂ via bimodal atomic force microscopy and finite element simulationYuhao Li^{1,2}, Chuanbin Yu^{1,2}, Yingye Gan³, Peng Jiang^{2,4}, Junxi Yu^{2,4}, Yun Ou^{2,5}, Dai-Feng Zou^{2,6}, Cheng Huang¹, Jiahong Wang⁷, Tingting Jia², Qian Luo⁸, Xue-Feng Yu⁷, Huijuan Zhao³, Cun-Fa Gao¹ and Jiangyu Li^{2,9}

Elasticity is a fundamental mechanical property of two-dimensional (2D) materials, and is critical for their application as well as for strain engineering. However, accurate measurement of the elastic modulus of 2D materials remains a challenge, and the conventional suspension method suffers from a number of drawbacks. In this work, we demonstrate a method to map the in-plane Young's modulus of mono- and bi-layer MoS₂ on a substrate with high spatial resolution. Bimodal atomic force microscopy is used to accurately map the effective spring constant between the microscope tip and sample, and a finite element method is developed to quantitatively account for the effect of substrate stiffness on deformation. Using these methods, the in-plane Young's modulus of monolayer MoS₂ can be decoupled from the substrate and determined as 265 ± 13 GPa, broadly consistent with previous reports though with substantially smaller uncertainty. It is also found that the elasticity of mono- and bi-layer MoS₂ cannot be differentiated, which is confirmed by the first principles calculations. This method provides a convenient, robust and accurate means to map the in-plane Young's modulus of 2D materials on a substrate.

npj Computational Materials (2018)4:49; doi:10.1038/s41524-018-0105-8

INTRODUCTION

Since the first successful exfoliation of graphene in 2004,¹ atomically thin two-dimensional (2D) materials such as graphene,^{2,3} hexagonal boron nitride (h-BN),⁴ transition metal dichalcogenides (TMDs)^{5–10} and black phosphorus (BP)^{11,12} have generated great excitement because of their unique and exotic functionalities.¹³ Of particular interest is the mechanical properties of 2D materials and structures, which are extremely stiff when stretched, yet exceptionally flexible in membrane form, and such extraordinary combination opens exciting opportunities for their engineering applications in microelectromechanical systems (MEMS) as well as flexible and stretchable electronics and photonics.^{14–17} Understanding the mechanical behavior of 2D materials also plays a central role in tuning their electronic and optoelectronic properties, wherein strain engineering can be highly effective.¹⁸ However, to date even the basic mechanical properties of most 2D materials, critical not only for device reliability but also for the emerging applications such as flexible electronics, remain largely uncharacterized and poorly understood, and it is still very challenging to accurately measure mechanical properties of 2D materials, especially when they are deposited on a substrate as in most devices instead of being suspended as in a testing structure.

To date, majorities of the mechanical testing of 2D materials follow the pioneering work of Hone et al.¹⁹ on graphene using

suspension method, wherein 2D samples suspended over pre-patterned holes are indented by atomic force microscope (AFM) probe, and the corresponding force–displacement curves obtained are analyzed within the frameworks of continuum mechanics.^{19–22} While having provided considerable insight into the mechanical properties of 2D materials, Young's modulus measured as such scatters over a large range and suffers from large uncertainty, for example 1000 ± 100 GPa for graphene,¹⁹ 270 ± 100 and 200 ± 60 GPa for mono- and bi-layer MoS₂,²⁰ and 330 ± 70 GPa for five-layer MoS₂.²¹ Note that there is substantial difference in Young's modulus between mono- and bi-layer MoS₂ measured, inconsistent with previous DFT calculations.²³ This is not unexpected since the method is based on the precise alignment of AFM probe with the center of the suspended membrane, which is very difficult to accomplish, and a slight misalignment will result in large errors. It is also nontrivial to fabricate the pre-patterned substrate and transfer the sample onto the designated holes, and mechanical properties measured from such suspended membrane may not be directly applicable to device structures, since for most applications 2D materials are usually directly deposited onto the substrate without suspension. In such case, spatial mappings of mechanical properties are highly desirable, for which the point-wise suspension method is inefficient, while the method to accurately map the mechanical

¹State Key Laboratory of Mechanics and Control of Mechanical Structures, Nanjing University of Aeronautics & Astronautics, Nanjing 210016 Jiangsu, China; ²Shenzhen Key Laboratory of Nanobiomechanics, Shenzhen Institutes of Advanced Technology, Chinese Academy of Sciences, Shenzhen, 518055 Guangdong, China; ³Department of Mechanical Engineering, Clemson University, Clemson, SC 29634-0921, USA; ⁴Key Laboratory of Low Dimensional Materials and Application Technology of Ministry of Education, School of Materials Science and Engineering, Xiangtan University, Xiangtan 411105 Hunan, China; ⁵Hunan Provincial Key Laboratory of Health Maintenance for Mechanical Equipment, Hunan University of Science and Technology, Xiangtan 411201 Hunan, China; ⁶School of Physics and Electronic Science, Hunan University of Science and Technology, Xiangtan 411201 Hunan, China; ⁷Institute of Biomedicine and Biotechnology, Shenzhen Institutes of Advanced Technology, Chinese Academy of Sciences, Shenzhen 518055 Guangdong, China; ⁸Shenzhen Institutes of Advanced Technology, Chinese Academy of Sciences, Shenzhen 518055 Guangdong, China and ⁹Department of Mechanical Engineering, University of Washington, Seattle, WA 98195, USA

Correspondence: Huijuan Zhao (hzhao2@clemson.edu) or C-F. Gao (cfgao@nuaa.edu.cn) or Jiangyu Li (jjli@uw.edu)

Received: 24 April 2018 Revised: 26 July 2018 Accepted: 6 August 2018

Published online: 29 August 2018

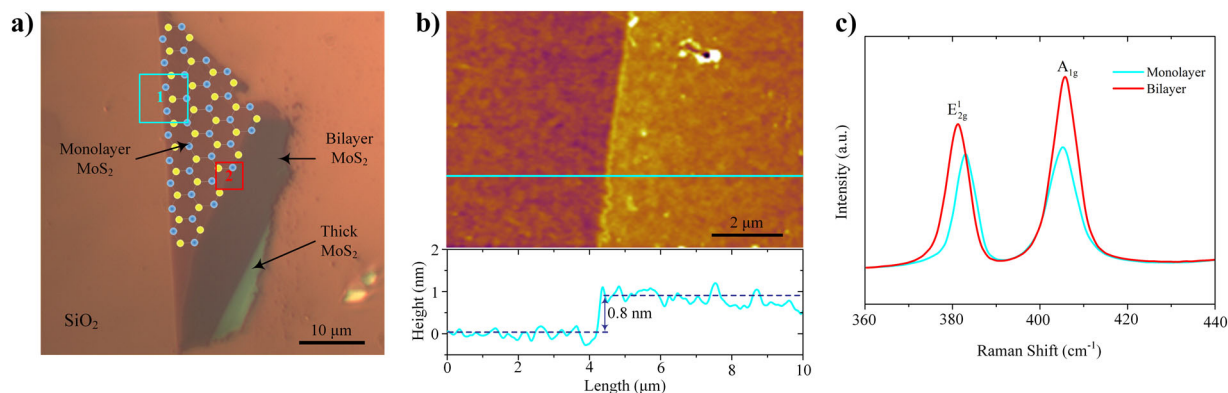


Fig. 1 Exfoliated MoS₂ on Si/SiO₂ substrate. **a** Optical image; **b** AFM topography mapping of cyan area marked in **a** with an interface between Si/SiO₂ and a monolayer MoS₂; **c** Raman spectra of mono- and bi-layer MoS₂

properties of 2D materials directly on the substrate with high spatial resolution and sensitivity has yet to be developed.

In this work, we demonstrate a method to map in-plane Young's modulus of 2D materials directly on the substrate with high spatial resolution, which can be easily applied to any 2D materials as processed, eliminating the need to transfer 2D samples onto pre-patterned substrate with holes. The method is also insensitive to the exact loading configuration and thus overcomes one of the major difficulties of suspension method, making the data robust with much less uncertainty. We demonstrate this method using mono- and bi-layer MoS₂, one of the most investigated 2D TMDs due to its excellent electronic properties.^{5,8,9,24} We apply bimodal AFM technique to accurately map the effective spring constant between the AFM tip and sample under both amplitude modulation (AM) and frequency modulation (FM),^{25,26} and then develop finite element method (FEM) to quantitatively account for the effect of substrate stiffness, which has substantial influence on the tip-sample interactions. As a result, the in-plane Young's modulus of MoS₂ can be decoupled from the substrate, and is determined to be 265 ± 13 GPa for monolayer, broadly consistent with previous reports yet with much smaller uncertainty. It is also found that the elasticity of mono- and bi-layer MoS₂ cannot be differentiated, which is supported by our DFT calculations showing virtually no interaction between the charges of S atoms on the top and bottom layers. The method thus provides a convenient, robust and accurate means to map the in-plane Young's modulus of 2D materials on a substrate, which can be easily applied to a wide range of materials and systems.

RESULTS

Mono- and bi-layer MoS₂

Mono- and bi-layer MoS₂ were micromechanically exfoliated from bulk MoS₂ crystal onto Si/SiO₂ substrate with 300 nm thick thermal oxide using Scotch tape, as detailed in Materials and Methods section,^{27,28} and the process is illustrated in Fig. S1 in the Supplementary Information (SI). The optical image of exfoliated MoS₂ is shown in Fig. 1a overlaid with a schematic MoS₂ lattice, wherein mono- and bi-layer as well as thicker MoS₂ can be seen judged from their distinct optic contrasts.²⁹ To confirm the layer counts, AFM scans in tapping mode were carried out over cyan box marked in Fig. 1a, with the resulting topography mappings in Fig. 1b showing a clear interface between MoS₂ and Si/SiO₂. The corresponding line scan of AFM topography reveals a step of approximately 0.8 nm high, and thus confirm monolayer MoS₂ in the corresponding region.³⁰ The red box marked in Fig. 1a exhibits an interface between mono- and bi-layer MoS₂, which will be examined later. These layer counts are further verified by Raman

measurements using 532 nm laser for excitation as detailed in Materials and Methods section, revealing peaks centered at 385.9 cm^{-1} and 405.4 cm^{-1} (red area) and 383.9 cm^{-1} and 405.4 cm^{-1} (cyan area) as shown in Fig. 1c, corresponding to out-of-plane (A_{1g}) and in-plane (E_{2g}^1) phonon modes of MoS₂, respectively. The differences of Raman shift between two peaks in cyan and red areas are 18.6 cm^{-1} and 21.5 cm^{-1} , respectively, confirming that there are monolayer and bilayer MoS₂.^{31–33} The Raman spectra excited by 633 nm laser were also obtained as shown in Fig. S2, revealing consistent data.

Bimodal atomic force microscopy (AM-FM)

We seek to map the elastic property of monolayer MoS₂ on Si/SiO₂ substrate quantitatively using bimodal AFM, which utilizes simultaneously the first and second flexural modes of the cantilever having spring constants k_1 and k_2 , with corresponding resonant frequencies f_1 and f_2 , amplitude A_1^0 and A_2^0 , and quality factors Q_1 and Q_2 under free vibration in air. When interacting with the sample in tapping mode during scanning, the cantilever has its first and second mode vibration amplitudes as well as first mode frequency preset at A_1 , A_2 , and f_1 , with the second mode kept at resonance by maintaining a constant phase ϕ_2 of $\pi/2$, as schematically shown in Fig. 2a.²⁶ Under such configuration, the first mode cantilever deflection is used to track the topography of the sample based on amplitude modulation (AM) with a large amplitude, and its amplitude A_1 and phase ϕ_1 are used to measure the tip-sample interaction stiffness. In addition, measuring the frequency shift Δf_2 of a higher eigenmode with a small amplitude A_2 based on frequency modulation (FM) provides complementary information about the tip-sample interaction. The method thus is referred to as AM-FM,^{25,34} which allows distinguishing between changes in indentation depth and sample modulus, and both of these independent measurements can be used to solve for the effective spring constant of the tip-sample system,³⁴

$$k_* = \pi \sqrt{\frac{2}{3}} \left(\frac{k_1 A_1^0}{Q_1 A_1} \cos \phi_1 \right)^{-1/2} \left(\frac{2k_2 \Delta f_2}{f_2 + \Delta f_2} \right)^{3/2}, \quad (1)$$

and the corresponding indentation depth δ during scanning is determined as^{25,34}

$$\delta = \frac{3}{4} \left(\frac{k_1 A_1^0 \cos \phi_1}{Q_1} \right) \left(\frac{2k_2 \Delta f_2}{f_2 + \Delta f_2} \right)^{-1}. \quad (2)$$

Note that the loss tangent of either first or second eigenmodes can be used to extract information about the dissipation at either of the frequencies f_1 and f_2 . As an example, mappings of phase ϕ_1 of the first flexural mode and frequency shift Δf_2 of the second flexural mode obtained from AM-FM scanning of monolayer MoS₂ on Si/SiO₂ substrate are shown in Fig. 2b, c, along with the

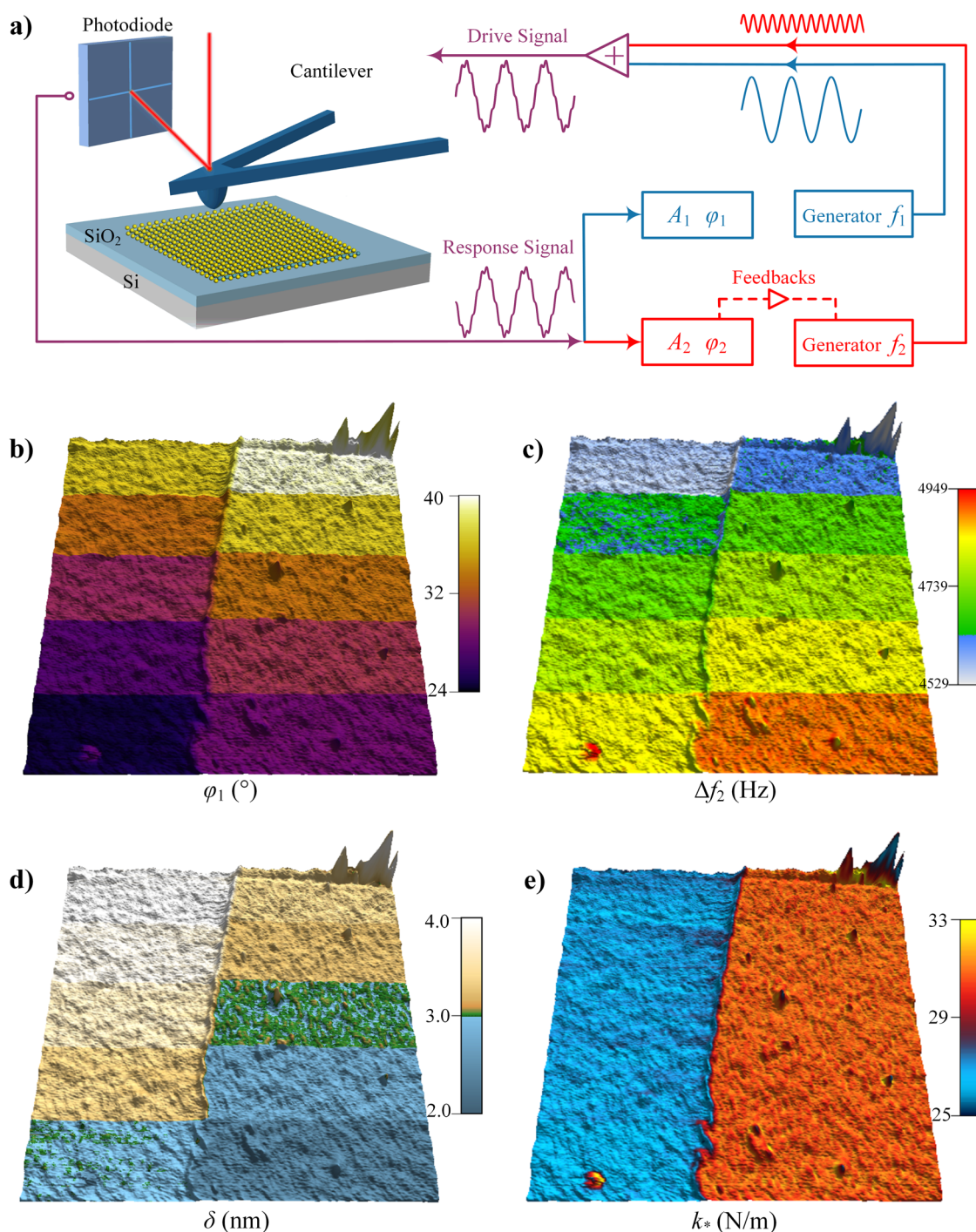


Fig. 2 AM-FM probing of monolayer MoS₂ on Si/SiO₂ substrate. **a** Schematic of AM-FM imaging; **b–d** mappings of **b** phase ϕ_1 of the first flexural mode, **c** frequency shift Δf_2 of the second flexural mode, and **d** maximum indentation depth δ , all overlaid on topography of monolayer MoS₂ (right) and Si/SiO₂ (left), with A_1 increased from 70 nm to 120 nm in 5 steps and the scan size of 5 μm ; and **e** corresponding effective spring constant k^* overlaid on topography

corresponding maximum indentation depth δ in Fig. 2d. During the scan, A_1 was increased incrementally from 70 nm to 120 nm in 5 steps, resulting in different phases, frequency shifts and indentation depths evident from these mappings, as expected from the theory.^{34,35} Nevertheless, the effective spring constant of the sample k^* calculated from Eq. (1) is stable and does not change under these different experimental conditions for both SiO₂ and MoS₂, as seen in Fig. 2e. While the intentional adjustment of set point results in horizontal bands in the mappings of phase

ϕ_1 , frequency shift Δf_2 , and indentation depth δ , the mapping of the effective spring constant only reveals a contrast between MoS₂ and SiO₂ without any bands, demonstrating that the method is robust and the effective spring constant measured is insensitive to the applied experimental parameters. Of particular interest is the indentation depth shown in Fig. 2d, in the range of a few nanometer. This is much smaller than 10% of the 300 nm thickness of SiO₂ as required for indentation test, and thus effective spring constant for SiO₂ is accurate. The depth, however,

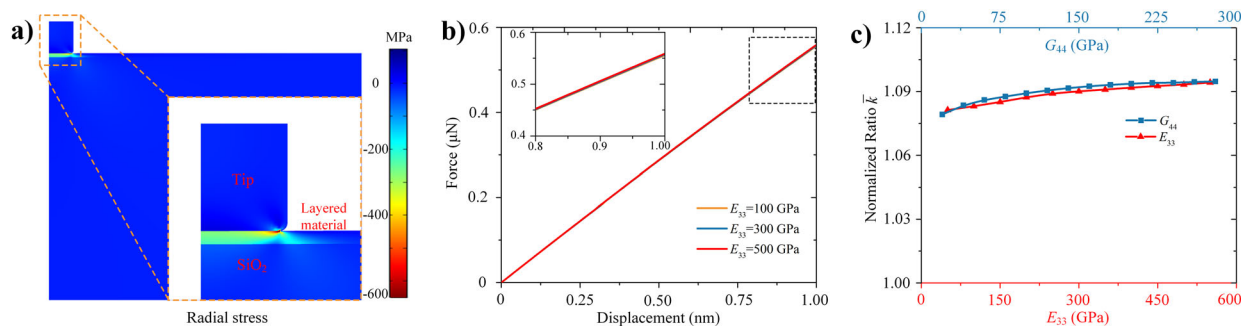


Fig. 3 FEM simulation of transversely isotropic layered material of different out-of-plane modulus on Si/SiO₂ substrate subjected to indentation by a silicon tip, with G_{44} and E_{11} of 50 and 300 GPa, respectively. **a** Radial stress distribution with E_{33} of 300 GPa; **b** force–displacement curves evaluated for different out-of-plane Young’s modulus; and **c** normalized effective spring constant \bar{k} evaluated under different out-of-plane Young’s modulus E_{33} and shear modulus G_{44}

is thicker than the thickness of MoS₂, and thus the effective spring constant mapped on MoS₂ reflects the influences of both MoS₂ and the underlying SiO₂. We thus resort to FEM based on contact mechanics to account for the effect of substrate and help us determine the intrinsic elastic property of monolayer MoS₂ from the mapping of effective spring constant.

Contact mechanics and finite element analysis

The effective spring constant measured from AM-FM makes it possible to determine Young’s modulus of the sample using contact mechanics theory. For a flat punch of radius R in contact with a homogeneous elastic material in half-space, the effective spring constant k_* is given by^{25,34,36}

$$k_* = 2RE_*, \quad (3)$$

such that the effective Young’s modulus E_* can be deduced from Eq. (1) as

$$E_* = \frac{\pi}{R} \sqrt{\frac{1}{6} \left(\frac{k_1 A_1^0}{Q_1 A_1} \cos \phi_1 \right)^{-1/2} \left(\frac{2k_2 \Delta f_2}{f_2 + \Delta f_2} \right)^{3/2}}, \quad (4)$$

with

$$\frac{1}{E_*} = \frac{1 - \nu_t^2}{E_t} + \frac{1 - \nu_s^2}{E_s} \quad (5)$$

where in E_t , E_s , ν_t and ν_s are Young’s modulus and Poisson’s ratio of tip and sample, respectively, from which Young’s modulus E_s of the sample can be determined. Note that explicitly characterizing geometrical shape of the tip is not necessary, since reference material with known Young’s modulus and Poisson’s ratio can be used for calibration instead to obtain the normalized effective spring constant \bar{k} of the sample with respect to that of reference material. In our case, Young’s modulus and Poisson’s ratio of SiO₂ are known, providing us a natural choice of reference for calibration. The effective spring constant of MoS₂ measured as such, however, is affected by the underlying SiO₂, and we thus resort to FEM to account for this effect. Such continuum analysis has proven to be appropriate for in-plane deformation of monolayer.^{20,21}

MoS₂ is a transversely isotropic layered material with five independent elastic constants,³⁷ namely in-plane and out-of-plane Young’s modulus E_{11} and E_{33} , in-plane and out-of-plane Poisson’s ratio ν_{12} and ν_{13} , and out-of-plane shear modulus G_{44} , as detailed in Materials and Methods section. Based on first-principles calculations and molecular dynamics simulations, Poisson’s ratios of MoS₂ can be assumed as 0.25.^{38–41} Hence, there are only three unknown material constants E_{11} , E_{33} and G_{44} to be determined. Note that we have ignored viscoelasticity in our current model, since the sample is stiff. The FEM model configuration is shown in Fig. 3a, wherein a transversely isotropic layered material with

thickness of 0.8 nm and radius of 150 nm on top of bulk SiO₂ substrate with thickness of 99.2 nm is indented by a flat punch made of silicon with radius of 5 nm, and the radial stress distribution in the probe and sample is shown when the tip press onto sample surface. What we are really interested in, however, is the slope of simulated force–displacement curve for direct comparison with AM-FM experiment, and it turns out that such curve is rather insensitive to the out-of-plane Young’s modulus E_{33} (Fig. 3b) and shear modulus G_{44} (Fig. S3a), wherein large changes in E_{33} and G_{44} results in no appreciable difference in force–displacement curve. This can be understood from the distribution of resulted in-plane and out-of-plane displacement versus radial distance away from the probe (Fig. S4), which shows that the in-plane displacement is much larger than out-of-plane displacement and its variation spans much larger regions, suggesting that the deformation mode is largely in-plane that justifies the continuum treatment. As a result, the normalized effective spring constant \bar{k} simulated shows little variation over large range of Young’s modulus E_{33} and shear modulus G_{44} (Fig. 3c), making it possible for us to determine E_{11} , regardless of E_{33} and G_{44} . We note that under flat punch approximation, the effective spring constant \bar{k} is insensitive to the tip radius for sufficient large computation domain and sufficient thick SiO₂, as shown in Fig. S5 and Fig. S6, and the effect of Si underneath of SiO₂ is negligible.

Because of insensitivity of force–displacement curve to out-of-plane modulus of 2D materials, it becomes possible to determine their in-plane Young’s modulus E_{11} from the AM-FM experiment. To appreciate this, we evaluated from FEM the force–displacement curves under different E_{11} with out-of-plane Young’s modulus E_{33} and shear modulus G_{44} set as 100 GPa and 50 GPa based on first-principles calculations of MoS₂,^{37,42} which shows distinct slope and thus k_* (Fig. 4a). The in-plane and out-of-plane displacement under different E_{11} confirms again that the dominant deformation mode is in-plane (Fig. 4b), and the normalized effective spring constant \bar{k} simulated for monolayer MoS₂ shows strong dependence on in-plane Young’s modulus E_{11} (Fig. 4c). Importantly, we can directly compare this curve of normalized effective spring constant \bar{k} with the experimentally measured data from different areas of sample and under different conditions, which falls into the reddish strip with \bar{k} measured between 1.0669 and 1.0795, which can be converted into in-plane Young’s modulus for monolayer MoS₂ using this curve.

Young’s modulus of mono- and bi-layer MoS₂

The relationship between the normalized effective spring constant \bar{k} and in-plane Young’s modulus E_{11} shown in Fig. 4c enables us to convert AM-FM mapping of the effective spring constant (Fig. 2e) into a mapping of Young’s modulus of MoS₂. To this end, the

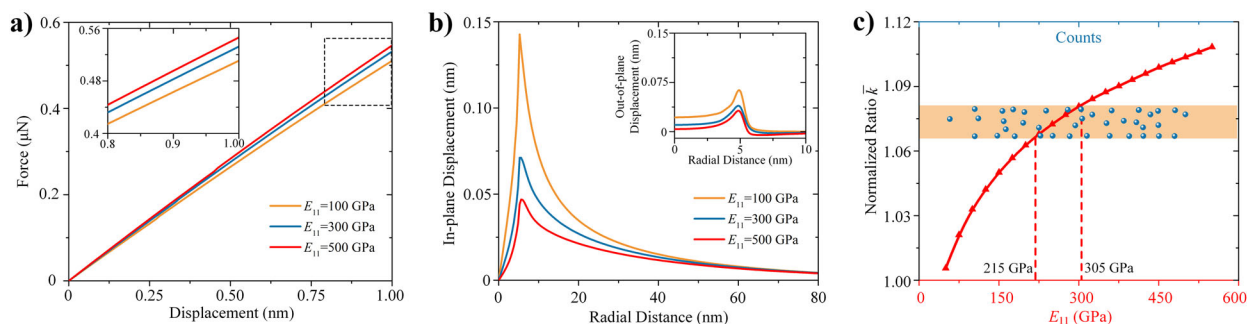


Fig. 4 FEM simulation of transversely isotropic layered material of different in-plane modulus on Si/SiO₂ substrate subjected to indentation by silicon tip, with E_{33} and G_{44} of 100 and 50 GPa, respectively. **a** Force–displacement curves evaluated for different in-plane Young's modulus; **b** in-plane and out-of-plane displacement on the surface of layered material; and **c** normalized effective spring constant \bar{k} simulated under different in-plane Young's modulus versus the experimental data

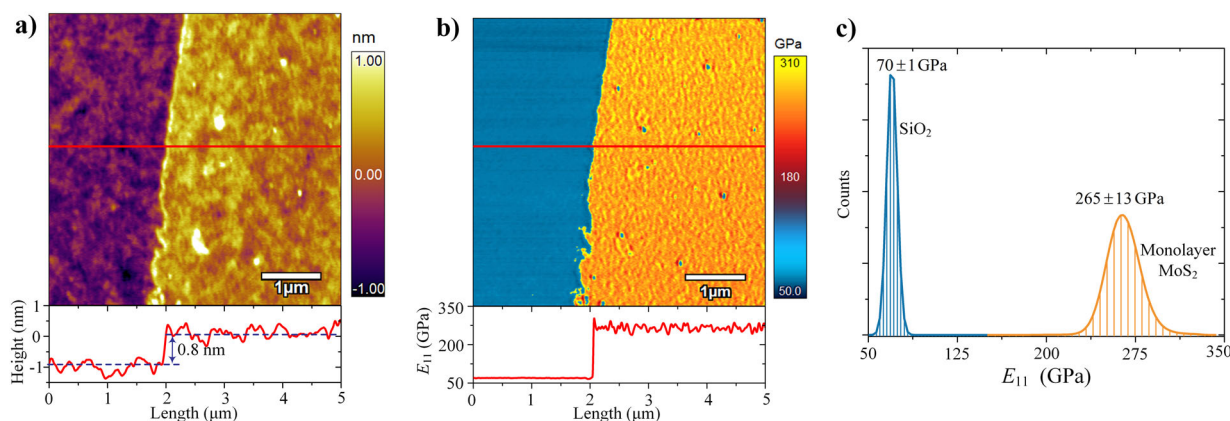


Fig. 5 In-plane Young's modulus of monolayer MoS₂ on Si/SiO₂, with mappings of **a** topography, **b** in-plane Young's modulus, and **c** histogram distribution of in-plane Young's modulus; the scan size is 5 μm

mappings of topography and in-plane Young's modulus obtained under the optimal experimental conditions are shown in Fig. 5a, b for monolayer MoS₂ and SiO₂, revealing distinct in-plane Young's modulus of monolayer MoS₂ and SiO₂. The corresponding histogram in Fig. 5c reveals that the distribution of in-plane Young's modulus is quite sharp, being 70 ± 1 GPa for SiO₂ and 265 ± 13 GPa for monolayer MoS₂, and it is consistent with earlier report yet with much smaller scattering.²⁰ As discussed, we used SiO₂ as a natural reference material for calibration, enabling us to carry out the analysis in just one mapping involving both monolayer MoS₂ and Si/SiO₂ substrate. While they have substantially different Young's modulus, the difference in indentation depth is rather small, as shown in Fig. S7, ensure the accuracy of AM-FM using reference method. Unlike the previous suspension method that derives Young's modulus at just a single point on micro-patterned substrate, our method allows spatial mapping of Young's modulus directly on an ordinary substrate, and thus it is particularly convenient for studying mechanical properties of 2D materials in a device configuration, wherein both substrate and/or interface, structural heterogeneity, and defects are important.

Of particular interest is Young's modulus of bilayer MoS₂, which is not expected to be different from that of monolayer due to weak van der Waals interactions between layers, yet previous study reported substantial difference, 270 ± 100 GPa for monolayer and 200 ± 60 GPa for bilayer.²⁰ We thus examined the red box in Fig. 1a that contains both mono- and bi-layer MoS₂, with its AFM topography shown in Fig. 6a revealing a clear 0.8 nm step between mono- and bi-layers. The AM-FM mapping of the effective spring constant in Fig. 6b, however, exhibits no appreciable difference between mono- and bi-layers, which is evident from the histogram distribution in Fig. 6c as well. To help

understand this result, we carry out the first-principles DFT calculation for bi-layer MoS₂, for which interlayer spacing h is a critical parameter. As seen from the charge density profile in Fig. 6d, there is a strong interaction between S atoms on the top and bottom layers at a small interlayer space of 1.50 Å, which becomes weaker and weaker with the increased h (Fig. S8). When h approaches 3.00 Å as shown in Fig. 6d, there is barely any interaction between the S atoms on the top and bottom layers, corresponding to weak van der Waals instead of covalent interaction between layers. Indeed, energetic analysis shows that the energy of bilayer MoS₂ per primitive cell decreases rapidly with increased h and converges to that of monolayer MoS₂ at around 3.00 Å, upon which the out-of-plane strain becomes zero and the energetic behavior is expected to be identical to that of monolayer MoS₂. As a result, the stress–strain curve and the corresponding Young's modulus of bilayer MoS₂ shown in Fig. 6e evaluated under the uniaxial loading converges with that of monolayer MoS₂, consistent with previous report.²³ In other words, the in-plane Young's modulus of perfect mono- and bi-layer MoS₂ are confirmed to be identical by DFT calculations, as observed in our AM-FM experiments.

DISCUSSION

Mechanical testing of 2D materials is highly challenging, and the main difficulty lies in the effect of substrate that imposes substantial influence on the mechanical response of 2D materials. Previous experimental efforts were primarily based on suspension method, requiring transferring of the sample onto substrates with pre-patterned holes, which is a nontrivial task. Even more importantly, such pointwise loading for force–displacement curve

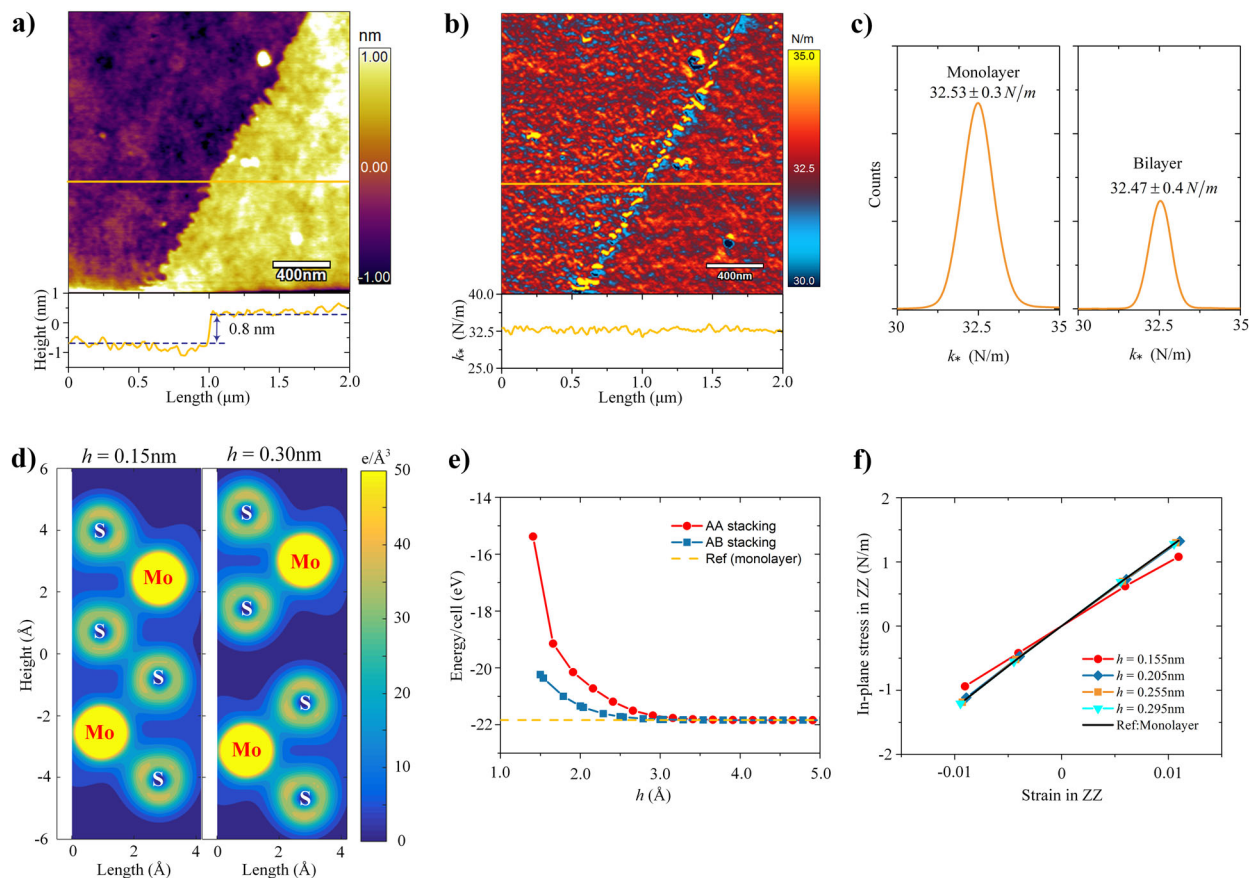


Fig. 6 In-plane Young's modulus of bi-layer MoS₂ interfacing with monolayer ones, with mappings of **a** topography, **b** effective spring constant k^* and **(c)** histogram distribution of effective spring constant k^* for mono- and bi-layer MoS₂, respectively; the scan size is 5 μm . **d** Charge density of bi-layer MoS₂ with respect to the interlayer space h ; **e** energetics of bi-layer MoS₂ with respect to the interlayer space; **f** stress–strain relation in Zigzag (ZZ) direction of bi-layer MoS₂ with difference interlayer spacing h

requires precise alignment of AFM at the symmetric center of the suspended membrane, or large error will be induced. This explains large scattering of experimentally reported data under suspension approach, up to 10% for graphene and 37% for monolayer MoS₂, since precise alignment is very difficult. Our method largely overcomes such difficulties. By mapping elastic response of 2D materials directly on the substrate using AM-FM, we eliminate the need of transferring the sample to pre-patterned substrate, and the precise alignment is no longer required as in a pointwise measurement, making the method widely applicable for other 2D materials and systems on any substrate, especially in a device configuration. The effect of substrate constraint is accurately accounted for by FEM, enabling us to decouple the deformation of 2D materials from the substrate. As a result, the in-plane Young's modulus of monolayer MoS₂ is measured to be 265 ± 13 GPa with less than 5% uncertainty, and that of bilayer MoS₂ is found to be indistinguishable from monolayer, which is rationalized by our DFT calculations. Importantly, it is the elasticity of 2D materials on the substrate instead of suspended one that is relevant for most applications, and the method provides a powerful technique to spatially map elasticity of 2D materials on the substrate with high resolution and sensitivity.

METHODS

Sample preparation

Mono- and few-layer of MoS₂ flakes were mechanically exfoliated from commercially available MoS₂ crystals (Graphene Supermarket) onto a Si substrate with a 300 nm SiO₂ layer using Scotch tape as the transfer medium, followed by annealing in argon at standard atmospheric pressure

and 350 °C for 1 h in order to enhance the contact between sample and substrate.²⁷ Before exfoliating, the substrates were ultrasonically cleaned in acetone, ethanol and deionized water, respectively, and then subjected to oxygen plasma for 10 min to remove ambient adsorbates from surface. The mechanical exfoliation process consists of following steps. The tape is pressed into contact with MoS₂ crystals by thumb first, and the thick MoS₂ flakes are stuck on the tape. The process is then repeated 4 or 5 times to thin the flakes, after which the substrate is pressed onto the tape with thin MoS₂ flakes for transferring. The obtained sample containing tape and substrates is packed by silver paper and put onto a hot plate to enhance contact between SiO₂ and MoS₂ for 3 min at 100 °C. Finally, the tape is removed from the substrates at approximately constant speed when the sample temperature is dropped to ambient temperature, which completes the exfoliation process, as illustrated in Fig. S1(a)–(f). While some tape residues may remain on the sample, as seen in the top right corner of Fig. 2b, clean areas can be found after careful search for further study.

Raman measurement

Raman scattering measurement was performed on a Horiba Jobin-Yvon LabRam HR-VIS high-resolution confocal Raman microscope equipped with a 532 nm laser and a 633 nm laser as the excitation source at room temperature to identify layer thickness of MoS₂ based on the difference between the out-of-plane vibrational (A_{1g}) and the in-plane vibration (E_{2g}^1) peaks, as reported by Lee et al.⁴³ A XYZ motorized sample stage controlled by LabSpec software was used to move sample accurately and the output power was controlled by neutral density filters to protect the MoS₂ samples.

Bimodal atomic force microscopy (AM-FM)

Bimodal atomic force microscopy (AM-FM) uses two driving forces with frequencies matching the first and the second flexural resonance of the

cantilever to excite the oscillation of probe. The tip deflection $z(t)$ can be written as follows,^{35,44} and the first two modes can be measured via lock-in.

$$z(t) = z_0 + \sum_n A_n \cos(\omega_n t - \phi_n) \quad (6)$$

$$\xrightarrow{\text{Lock-in}} z_0 + A_1 \cos(\omega_1 t - \phi_1) + A_2 \cos(\omega_2 t - \frac{\pi}{2}).$$

In Eq. (6) A_n , ϕ_n , and $\omega_n = 2\pi f_n$ are amplitude, phase and angular frequency of n th mode. During the experiment, the cantilever parameters k_1 , k_2 , f_1 , f_2 , Q_1 , and Q_2 are determined by fitting the thermal signals of the cantilever away from the surface before experiment, and the sensitivity of the optical beam deflection is deduced from the force–displacement curve obtained when approaching a hard sample.⁴⁵ Before tip–sample interaction, the probe is driven close to its first resonant frequency f_1 with a large amplitude A_1^0 (~100 nm) and its second resonant frequency f_2 with a small amplitude A_2^0 (~1 nm) in air. Upon approaching the sample, the responses of the two resonance frequencies are tracked by two independent lock-in amplifiers. For the first flexural resonance mode, the frequency f_1 , amplitude A_1 and the phase ϕ_1 are extracted from the deflection signal of the probe and the feedback makes adjustment to keep a predetermined amplitude set point A_1 . Meanwhile, the feedback for the second flexural mode adjusts the frequency by a small shift Δf_2 to maintain the phase ϕ_2 of the second flexural mode at $\pi/2$ with a constant amplitude set point A_2 . This makes sure the amplitude A_2 of the second flexural mode is considerable compared to the noise while relatively small compared to the indentation depth δ ,²⁵ as shown in Fig. S9.

Our AM-FM experiments were performed on Asylum Research MFP-3D atomic force microscope in ambient using OMCL-AC160TS-R3 probe with $k_1 = 31.19$ N/m, $f_1 = 283.58$ kHz, $k_2 = 996.30$ N/m, and $f_2 = 1.60$ MHz in air. For monolayer MoS₂, the free amplitudes were $A_1^0 = 260$ nm and $A_2^0 = 5$ nm, and the image was taken at $A_1 = 100$ nm. For bilayer MoS₂, the experimental values for the probe were $k_1 = 42.20$ N/m, $f_1 = 301.41$ kHz, $k_2 = 1358.3$ N/m, and $f_2 = 1.70$ MHz in air. The free amplitudes were $A_1^0 = 186$ nm and $A_2^0 = 5$ nm, and the image was taken at $A_1 = 56$ nm. Note that assumed Euler-Bernoulli dynamic stiffness scaling for AC160 cantilever, where $k_2 = k_1(f_2/f_1)^2$. As shown in ref.⁴⁵, due to the presence of probe tip and/or not ideal thin diving boards, the scaling exponent for an AC160 was actually found to be ~1.67. Nevertheless, our analysis indicating that different scaling exponents have negligible influence on the results, as shown in Fig. S10, which is also consistent with earlier report by Kocun et al.²⁵

FEM simulation

Transversely isotropy layered material is considered, with elastic matrix given by^{46,47}

$$C^{-1} = \begin{bmatrix} 1/E_{11} & -\nu_{12}/E_{11} & -\nu_{13}/E_{33} & 0 & 0 & 0 \\ -\nu_{12}/E_{11} & 1/E_{11} & -\nu_{13}/E_{33} & 0 & 0 & 0 \\ -\nu_{13}/E_{33} & -\nu_{13}/E_{33} & 1/E_{33} & 0 & 0 & 0 \\ 0 & 0 & 0 & 1/G_{44} & 0 & 0 \\ 0 & 0 & 0 & 0 & 1/G_{44} & 0 \\ 0 & 0 & 0 & 0 & 0 & 2(1 + \nu_{12})/E_{11} \end{bmatrix} \quad (7)$$

COMSOL Multiphysics software was chosen to simulate this problem because of its parametric modeling. In order to save computing time, a central symmetry model was developed, consisting of cantilever tip (punch), layered material and substrate as shown in Fig. 3a. The height and radius are 7.5 nm and 5 nm for tip, 0.8 nm and 150 nm for layered material, and 99.2 nm and 150 nm for substrate, respectively. The material of cantilever tip and substrate are silicon and silicon dioxide with respective Poisson's ratio and Young's modulus of 0.28 and 170 GPa for silicon and 0.17 and 70 GPa for silicon dioxide. For convergence and simplification, the displacement instead of force of tip was selected as 'Loads', which is defined by pressing the tip into sample surface for 1 nm under 100 steps for each trace and retrace. An eight-node rectangular unit was used as basic element of mesh, and convergence test were carried out by changing the number of elements, as shown in Fig. S11.

DFT calculations

First-principles DFT calculations were carried out using the Vienna Ab initio Simulation Package (VASP).^{48,49} We adopt the PAW pseudopotential⁵⁰ for electron–ionic core interaction and the generalized gradient

approximation (GGA) for the electron exchange and correlation with the Perdew–Burke–Ernzerhof (PBE)⁵¹ formulation. We also use the conjugate-gradient algorithm for ion relaxation with the cutoff energy set at 300 eV. As shown in Fig. S12, we consider monolayer MoS₂ and bi-layer MoS₂ with AA stacking and AB stacking, respectively. Periodic boundary condition is applied with a vacuum region of 40 Å along the out-of-plane direction to avoid the inter-layer interactions. A primitive cell in all the cases is adopted for the calculation. A K -point mesh of $16 \times 16 \times 1$ is used with the Monkhorst–Pack sampling scheme.

DATA AVAILABILITY

The data and code used in this study are available from the corresponding author upon request.

ACKNOWLEDGEMENTS

We acknowledge National Key Research and Development Program of China (2016YFA0201001), National Natural Science Foundation of China (11627801, 11232007, 11472130, 11472236, and 51702351), Shenzhen Science and Technology Innovation Committee (KQJSCX20170331162214306, JCYJ20170413152832151, JCYJ20170818160815002), US National Science Foundation (CBET-1435968), the Leading Talents Program of Guangdong Province (2016LJ06C372), and Shenzhen Programs for Science and Technology Development (JSGG20160229204218661).

AUTHOR CONTRIBUTIONS

J.L. and C.-F.G. conceived and designed the project. Y.L., Y.O., D.-F.Z. and T.J. performed the material fabrication. Y.L., P.J., and J.Y. carried out the AFM experiments and analyses under J.L.'s guidance. J.W., X.-F.Y. and Q.L. carried out the Raman experiments and analyses. C.Y., C.H., and Y.L. carried out FEM calculations and analyses under C.-F.G.'s guidance. H.Z. and Y.G. carried out DFT calculations and analyses. J.L., Y.L., C.Y., H.Z., and C.-F.G. wrote the paper, and all authors contributed to the discussions and preparation of the manuscript.

ADDITIONAL INFORMATION

Supplementary information accompanies the paper on the *npj Computational Materials* website (<https://doi.org/10.1038/s41524-018-0105-8>).

Competing interests: The authors declare no competing interests.

Publisher's note: Springer Nature remains neutral with regard to jurisdictional claims in published maps and institutional affiliations.

REFERENCES

- Novoselov, K. S. et al. Electric field effect in atomically thin carbon films. *Science* **306**, 666–669 (2004).
- Geim, A. K. Graphene: status and prospects. *Science* **324**, 1530–1534 (2009).
- Mas-Balleste, R., Gomez-Navarro, C., Gomez-Herrero, J. & Zamora, F. 2D materials: to graphene and beyond. *Nanoscale* **3**, 20–30 (2011).
- Dean, C. R. et al. Boron nitride substrates for high-quality graphene electronics. *Nat. Nanotechnol.* **5**, 722–726 (2010).
- Mak, K. F., Lee, C., Hone, J., Shan, J. & Heinz, T. F. Atomically thin MoS₂: a new direct-gap semiconductor. *Phys. Rev. Lett.* **105**, 136805 (2010).
- Xu, X., Yao, W., Xiao, D. & Heinz, T. F. Spin and pseudospins in layered transition metal dichalcogenides. *Nat. Phys.* **10**, 343–350 (2014).
- Chhowalla, M. et al. The chemistry of two-dimensional layered transition metal dichalcogenide nanosheets. *Nat. Chem.* **5**, 263–275 (2013).
- Radisavljevic, B., Radenovic, A., Brivio, J., Giacometti, V. & Kis, A. Single-layer MoS₂ transistors. *Nat. Nanotechnol.* **6**, 147–150 (2011).
- Wang, Q. H., Kalantar-Zadeh, K., Kis, A., Coleman, J. N. & Strano, M. S. Electronics and optoelectronics of two-dimensional transition metal dichalcogenides. *Nat. Commun.* **7**, 699–712 (2012).
- Balendhran, S. et al. Two-dimensional molybdenum trioxide and dichalcogenides. *Adv. Funct. Mater.* **23**, 3952–3970 (2013).
- Li, L. et al. Black phosphorus field-effect transistors. *Nat. Nanotechnol.* **9**, 372–377 (2014).
- Liu, H. et al. Phosphorene: an unexplored 2D semiconductor with a high hole mobility. *ACS Nano* **8**, 4033–4041 (2014).
- Tan, C. et al. Recent advances in ultrathin two-dimensional nanomaterials. *Chem. Rev.* **117**, 6225–6331 (2017).

14. Tu, Q. et al. Quantitative subsurface atomic structure fingerprint for 2D materials and heterostructures by first-principles-calibrated contact-resonance atomic force microscopy. *ACS Nano* **10**, 6491–6500 (2016).
15. Bhimanapati, G. R. et al. Recent advances in two-dimensional materials beyond graphene. *ACS Nano* **9**, 11509–11539 (2015).
16. Kalinin, S. V. et al. Big, deep, and smart data in scanning probe microscopy. *ACS Nano* **10**, 9068–9086 (2016).
17. Xie, C., Mak, C., Tao, X. & Yan, F. Photodetectors based on two-dimensional layered materials beyond graphene. *Adv. Funct. Mater.* **27**, 1–14 (2017).
18. Xie, C. & Yan, F. Flexible photodetectors based on novel functional materials. *Small* **13**, 1–36 (2017).
19. Lee, C., Wei, X., Kysar, J. W. & Hone, J. Measurement of the elastic properties and intrinsic strength of monolayer graphene. *Science* **321**, 385–388 (2008).
20. Bertolazzi, S., Brivio, J. & Kis, A. Stretching and breaking of ultrathin MoS₂. *ACS Nano* **5**, 9703–9709 (2011).
21. Castellanos-Gomez, A. et al. Elastic properties of freely suspended MoS₂ nanosheets. *Adv. Mater.* **24**, 772–775 (2012).
22. Frank, I. W., Tanenbaum, D. M., Zande van der, A. M. & McEuen, P. L. Mechanical properties of suspended graphene sheets. *J. Vac. Sci. Technol. B Microelectron. Nanom. Struct.* **25**, 2558–2561 (2007).
23. Mukhopadhyay, T., Mahata, A., Adhikari, S. & Zaeem, M. A. Effective mechanical properties of multilayer nano-heterostructures. *Sci. Rep.* **7**, 1–13 (2017).
24. Rogers, J. A., Someya, T. & Huang, Y. Materials and mechanics for stretchable electronics. *Science* **327**, 1603–1607 (2010).
25. Kocun, M., Labuda, A., Meinhold, W., Revenko, I. & Proksch, R. Fast, high resolution, and wide modulus range nanomechanical mapping with bimodal tapping mode. *ACS Nano*. <https://doi.org/10.1021/acsnano.7b04530> (2017).
26. Garcia, R. & Herruzo, E. T. The emergence of multifrequency force microscopy. *Nat. Nanotechnol.* **7**, 217–226 (2012).
27. Huang, Y. et al. Reliable exfoliation of large-area high-quality flakes of graphene and other two-dimensional materials. *ACS Nano* **9**, 10612–10620 (2015).
28. Late, D. J., Liu, B., Matte, H. S. S. R., Rao, C. N. R. & Dravid, V. P. Rapid characterization of ultrathin layers of chalcogenides on SiO₂/Si substrates. *Adv. Funct. Mater.* **22**, 1894–1905 (2012).
29. Benameur, M. M. et al. Visibility of dichalcogenide nanolayers. *Nanotechnology* **22**, 125706 (2011).
30. Li, H. et al. Optical identification of single- and few-layer MoS₂ sheets. *Small* **8**, 682–686 (2012).
31. Geim, A. K. & Novoselov, K. S. The rise of graphene. *Nat. Mater.* **6**, 183 (2007).
32. Rodríguez, T. R. & García, R. Compositional mapping of surfaces in atomic force microscopy by excitation of the second normal mode of the microcantilever. *Appl. Phys. Lett.* **84**, 449–451 (2004).
33. Li, H. et al. From bulk to monolayer MoS₂: evolution of Raman scattering. *Adv. Funct. Mater.* **22**, 1385–1390 (2012).
34. Labuda, A., Kocun, M., Meinhold, W., Walters, D. & Proksch, R. Generalized Hertz model for bimodal nanomechanical mapping. *Beilstein J. Nanotechnol.* **7**, 970–982 (2016).
35. Amo, C. A., Perrino, A. P., Payam, A. F. & Garcia, R. Mapping elastic properties of heterogeneous materials in liquid with Angstrom-scale resolution. *ACS Nano* **11**, 8650–8659 (2017).
36. Sneddon, I. N. The relation between load and penetration in the axisymmetric Boussinesq problem for a punch of arbitrary profile. *Int. J. Eng. Sci.* **3**, 47–57 (1965).
37. Pan, Y. & Guan, W. Effect of sulfur concentration on structural, elastic and electronic properties of molybdenum sulfides from first-principles. *Int. J. Hydrog. Energy* **41**, 11033–11041 (2016).
38. Yue, Q. et al. Mechanical and electronic properties of monolayer MoS₂ under elastic strain. *Phys. Lett. A* **376**, 1166–1170 (2012).
39. Hess, P. Prediction of mechanical properties of 2D solids with related bonding configuration. *RSC Adv.* **7**, 29786–29793 (2017).
40. Xiong, S. & Cao, G. Molecular dynamics simulations of mechanical properties of monolayer MoS₂. *Nanotechnology* **26**, 185705 (2015).
41. Gan, Y. & Zhao, H. Chirality effect of mechanical and electronic properties of monolayer MoS₂ with vacancies. *Phys. Lett. Sect. A Gen. At. Solid State Phys.* **378**, 2910–2914 (2014).
42. Li, J., Medhekar, N. V. & Shenoy, V. B. Bonding charge density and ultimate strength of monolayer transition metal dichalcogenides. *J. Phys. Chem. C* **117**, 15842–15848 (2013).
43. Lee, C. et al. Anomalous lattice vibrations of single- and few-layer MoS₂. *ACS Nano* **4**, 2695–2700 (2010).
44. Garcia, R. & Proksch, R. Nanomechanical mapping of soft matter by bimodal force microscopy. *Eur. Polym. J.* **49**, 1897–1906 (2013).
45. Labuda, A. et al. Calibration of higher eigenmodes of cantilevers. *Rev. Sci. Instrum.* **87**, 73705 (2016).
46. Lekhnitskiĭ, S. G. *Theory of Elasticity of Anisotropic Body* (Mir Publishers, Moscow, 1981).
47. Ding, H., Chen, W. & Zhang, L. *Elasticity of Transversely Isotropic Materials* (Springer, Netherlands, 2006).
48. Kresse, G. & Furthmüller, J. Efficient iterative schemes for ab initio total-energy calculations using a plane-wave basis set. *Phys. Rev. B - Condens. Matter Mater. Phys.* **54**, 11169–11186 (1996).
49. Kresse, G. & Joubert, D. From ultrasoft pseudopotentials to the projector augmented-wave method. *Phys. Rev. B Condens. Matter* **59**, 1758–1775 (1999).
50. PE, B. Projector augmented-wave method. *Phys. Rev. B Condens. Matter* **50**, 17953 (1994).
51. Perdew, J. P., Burke, K. & Ernzerhof, M. Generalized gradient approximation made simple. *Phys. Rev. Lett.* **77**, 3865–3868 (1996).



Open Access This article is licensed under a Creative Commons Attribution 4.0 International License, which permits use, sharing, adaptation, distribution and reproduction in any medium or format, as long as you give appropriate credit to the original author(s) and the source, provide a link to the Creative Commons license, and indicate if changes were made. The images or other third party material in this article are included in the article's Creative Commons license, unless indicated otherwise in a credit line to the material. If material is not included in the article's Creative Commons license and your intended use is not permitted by statutory regulation or exceeds the permitted use, you will need to obtain permission directly from the copyright holder. To view a copy of this license, visit <http://creativecommons.org/licenses/by/4.0/>.

© The Author(s) 2018